Journal of
Synchrotron
Radiation

ISSN 1600-5775

Received 29 August 2014
Accepted 24 November 2014

Pushing the limits: an instrument for hard X-ray imaging below 20 nm

E. Nazaretski,[a] K. Lauer,[a] H. Yan,[a] N. Bouet,[a] J. Zhou,[a] R. Conley,[a,b] X. Huang,[a] W. Xu,[a] M. Lu,[a] K. Gofron,[a] S. Kalbfleisch,[a] U. Wagner,[c] C. Rau[c] and Y. S. Chu[a]*

[a]Brookhaven National Laboratory, Upton, NY, USA, [b]Advanced Photon Source, Argonne National Laboratory, Argonne, IL, USA, and [c]Diamond Light Source Ltd, Didcot, Oxfordshire OX11 0DE, UK. *E-mail: ychu@bnl.gov

Hard X-ray microscopy is a prominent tool suitable for nanoscale-resolution non-destructive imaging of various materials used in different areas of science and technology. With an ongoing effort to push the 2D/3D imaging resolution down to 10 nm in the hard X-ray regime, both the fabrication of nano-focusing optics and the stability of the microscope using those optics become extremely challenging. In this work a microscopy system designed and constructed to accommodate multilayer Laue lenses as nanofocusing optics is presented. The developed apparatus has been thoroughly characterized in terms of resolution and stability followed by imaging experiments at a synchrotron facility. Drift rates of $\sim$2 nm h^{-1} accompanied by 13 nm $\times$ 33 nm imaging resolution at 11.8 keV are reported.

Keywords: scanning X-ray microscopy; multilayer Laue lenses; interferometry; nanopositioning.

1. Introduction

Imperative for a fundamental understanding of materials is our ability to design, manipulate and control their ultimate functionalities. To understand and develop materials by design, determination of nanoscale-level chemical composition and nanoscale visualization become critical. Hard X-ray imaging is an excellent tool for revealing internal structures of nano-electronic devices, materials used for catalysis and functional materials, for example. The large penetration depth of hard X-rays allows non-destructive mapping of internal properties and structures (Ice *et al.*, 2011). Fresnel X-ray zone plates (Wu *et al.*, 2012; Chen *et al.*, 2011; Vila-Comamala *et al.*, 2011; Bukhard *et al.*, 2011), compound refractive lenses (Schroer *et al.*, 2005), kinoform refractive lenses (Evans *et al.*, 2007), multilayer Laue lenses (MLLs) (Kang *et al.*, 2006; Yan *et al.*, 2011, 2014; Huang *et al.*, 2013) and Kirkpatrick–Baez (KB) elliptical mirrors (Mimura *et al.*, 2010) have been used to achieve nanofocusing. Each of these nanofocusing elements has its own advantages and disadvantages; however, all of them require a dedicated apparatus suitable for alignment and performing nanoscale imaging. In this work we present an X-ray microscope designed and constructed to accommodate MLL nanofocusing optics and demonstrate the performance of the system through laboratory characterization and imaging experiments at a synchrotron facility with 13 nm $\times$ 33 nm spatial resolution at 11.8 keV.

2. Design of the MLL microscope

Using MLL diffractive optics is one of the routes to achieve nanofocusing in the hard X-ray regime (Yan *et al.*, 2011, 2014). As an MLL is a one-dimensional focusing element, achieving a point focus requires two such optics to be oriented orthogonally to one another, similar to KB mirrors. When fully aligned, the Bragg condition has to be satisfied for both focusing elements (Yan *et al.*, 2014). A schematic of the MLL microscope is shown in Fig. 1(*a*), and all major components and required degrees of motion for each of these components are depicted. As shown in Fig. 1(*a*), to perform a full MLL alignment there is a need for five translational and three rotational degrees of motion. Moreover, working distances for MLL optics are extremely small, of the order of a few millimeters for 10 keV energy, 50 µm MLL aperture and 10 nm width of the outermost zone. These requirements (multiple degrees of motion and short working distances) pose a challenge for designing of an apparatus capable of performing scanning measurements, and at the same time providing adequate stability to minimize vibrations and reduce possible thermal drifts. Though previous MLL systems demonstrated excellent performance, they had a large footprint, were not vacuum compatible and were not equipped with interferometric feedback for enhanced stability (Nazaretski *et al.*, 2013, 2014; Shu *et al.*, 2013), all of which are essential when enhanced functionality of a system is required. Therefore, to enable in-vacuum performance, provide enough stability and reduce thermal drifts, the apparatus shown in Figs. 1(*a*) and

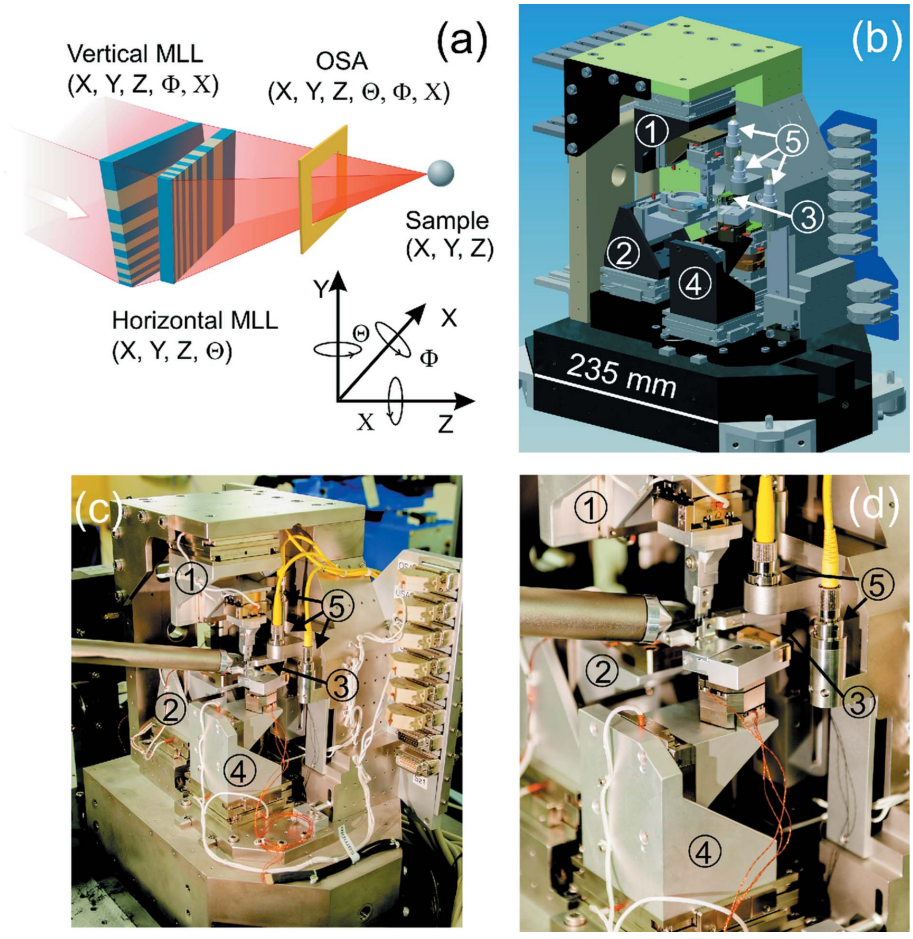

Figure 1
(*a*) Schematic of the MLL microscope. All required motions for individual components are shown. (*b*) CAD model of the MLL microscope. (*c*) Photograph of the assembled microscope, key components are enumerated: 1, vertical MLL assembly; 2, horizontal MLL assembly; 3, OSA assembly; 4, sample stage; 5, fiber optic interferometers heads. (*d*) Zoom-in of a sample area.

1(*b*) has been designed and constructed. This microscope greatly relies on the principles used in scanning probe microscopy systems which employ a small form factor, low heat dissipation, stiff piezo actuators and at the same time achieve excellent spatial resolution (Mesaros *et al.*, 2011; Nazaretski *et al.*, 2009; Meckler *et al.*, 2009; Lammle *et al.*, 2010). Following these principles, we built the MLL microscope which employs only piezo actuators. A schematic of this microscope, a computer-aided design (CAD) model and photographs of the actual system are shown in Fig. 1(*d*), with all major components enumerated. The microscope consists of different functional modules, *i.e.* 1, the vertical MLL assembly; 2, the horizontal MLL assembly; 3, the OSA assembly; 4, the sample stage assembly. The sample stage is used for scanning fluorescence, scanning differential phase contrast (DPC) and ptychography measurements. Each of the microscope modules is equipped with different types of standard and customized piezo stages manufactured by Attocube AG, Smaract GmbH and PI/Micos GmbH. In total, the microscope comprises 20 various piezo-motors providing fluorescence, ptychography and DPC imaging capabilities. For fine sample scanning, piezo scanners with built-in flexure amplifiers are mounted on top of coarse stick-slip stages and enable imaging in a 50 µm × 50 µm × 50 µm volume. To track the position of individual components and ensure adequate compensation of all thermal drifts, a total of nine fiber-optic interferometers monitor the *X*, *Y* and *Z* positions of the vertical, horizontal MLL and sample assemblies. Mounted on a common Invar reference frame, all interferometer heads (AttoFPSensors; see Nazaretski *et al.*, 2013 for characterization details) monitor the displacements/drifts of components in close proximity to the sample and MLL optics positions. In Fig. 1(*c*) it can be seen that for the sample stage (labeled 4 in the figure) reflectors are mounted within 10 mm from the sample location.

The control system of the MLL microscope is based on the Experimental Physics and Industrial Control System (EPICS), which allows inter-device communication and control over the network by way of the EPICS Channel Access protocol. A simple command-line interpreter named ECLI was developed on top of IPython, offering the full power of Python integrated with the EPICS devices in the system. Usage of the StepScan library allows for scans to be performed on all motors in the system, with the acquired data output to either HDF5 or a human-readable (ASCII) format. Scan progress can then be visualized with a simple Matplotlib-based client, or alternatively the PyMca X-ray fluorescence toolkit. The Delta Tau Power PMAC, a Linux-based motion control system featuring the Xenomai real-time kernel, is the core of the motion control system. An extended PID (including feed-forward terms) locks the *X*, *Y*, *Z* fine sample piezo scanner into position in accordance with the AttoFPSensor interferometers digital quadrature encoder feedback. Combining the high-resolution digital-to-analog converter of the Power PMAC with the low-noise attocube ANC200 piezo amplifier, robust sub-nanometer positioning has been achieved (Gofron *et al.*, 2014). All detectors in the system were triggered by the Struck SIS3820 VME scaler. During synchrotron characterization experiments, fluorescence data were acquired *via* the Quantum Detectors Xspress 3 readout system and a Ketek fluorescence detector. Transmitted beam data for ptychographic reconstructions and DPC data were acquired with the TimePix QTPX-262k detector from Amsterdam Scientific Instruments. DPC calculations were performed using only Python and NumPy, parallelized with the multiprocessing library.

3. Preliminary characterization of the microscope

Following its design and construction, the instrument went through a thorough laboratory characterization prior to installation and testing at the beamline. Results of some of the tests performed are summarized in Fig. 2. For resolution measurements the instrument was placed inside the vacuum chamber in the Nanopositioning Laboratory at NSLS-II (see Fig. 2*a*) with a corresponding vacuum level of $\sim 10^{-6}$ mbar. The sample stage was moved with 0.5 nm increments (see Fig. 2*c*). The RMS background noise observed equals $\sim$0.35 nm and 0.5 nm steps were clearly resolved. The background noise is consistent with noise levels demonstrated earlier on stiff test structures (see Nazaretski *et al.*, 2013), and confirms the stability of the microscope with minimal amplification of environmental vibrations.

Uncompensated thermal drifts of a sample or nanofocusing optics are primary contributors to image distortions observed during scanning X-ray microscopy experiments. Stick-slip stages used in the microscope do not generate any heat when not in motion; therefore, primary heat sources reside inside optoelectronic encoders used in the majority of nano-stages. A typical optoelectronic encoder dissipates between 200–300 mW of heat which in our case results in 5–5.75 W of heat being dissipated inside the vacuum chamber. Such a significant amount of heat results in longer thermalization times and consequently may delay data acquisition after a sample has been placed inside a vacuum chamber. To overcome excessive heat dissipation, the duty-cycling technique has been used. When not in motion (or potentially all of the time), encoders of nano-stages can be power cycled to be in operation for only 1–10% of the time. The period of duty-cycling is bound by the required speed of motion and is directly proportional to heat dissipation. Duty-cycling mode allows for the reduction of the overall heat dissipation to less than 500 mW for the entire instrument. Figs. 2(*d*) and 2(*f*) demonstrate the effect of duty-cycling. In both panels of the figure an infrared image of the vertical MLL assembly is also shown (acquired with a FLIR A655sc infrared camera). The vertical MLL assembly consists of three linear stages and two tip/tilt goniometers [an actual photograph is shown in Fig. 2(*b*)]. Panel (*d*) in Fig. 2 shows a thermal image of the vertical MLL assembly when all encoders are enabled 100% of the time. Fig. 2(*f*) shows a thermal image of the stage when duty-cycling was enabled and encoders were activated only 1% of the time. From Fig. 2(*d*) it is clear that heat sources are located around encoders incorporated in bodies of nanopositioning stages and thermal differences exceed 8 K between measurement points. When duty-cycling was enabled, thermal gradients were reduced by an order of magnitude and most of the temperature difference

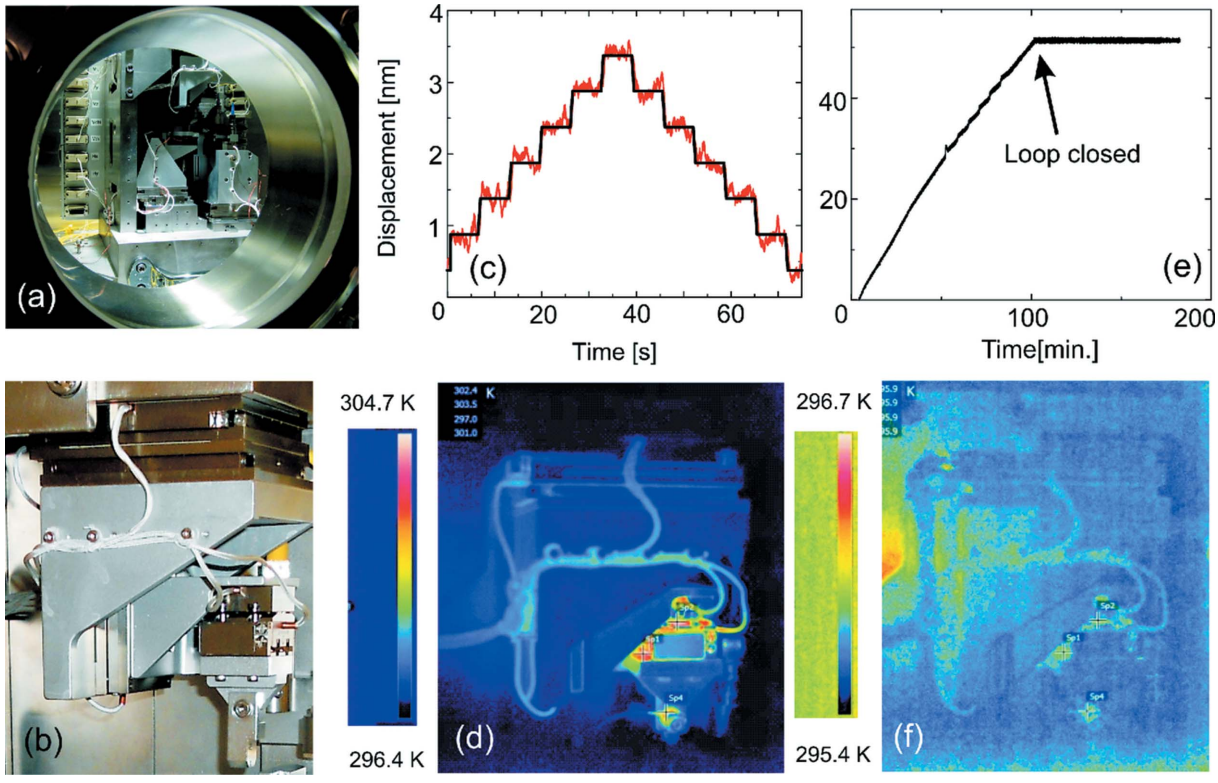

Figure 2
Laboratory characterization of the MLL microscope. (*a*) The MLL microscope inside a vacuum chamber during testing procedures; (*c*) resolution measurements, 0.5 nm steps performed with a sample stage, the red line showing interferometer readings, the black line representing the desired motion trajectory; (*e*) drift of the sample stage measured using interferometry in the open/closed loop mode of operation, interferometer readings are independent of motion controls system; (*b*), (*d*), (*f*) thermal profile measurements: (*b*) photograph of the vertical MLL assembly, (*d*) infrared image of the vertical MLL assembly, encoders are powered all the time, (*f*) vertical MLL assembly with duty-cycling mode enabled, thermal gradients diminished significantly.

originates from thermal reflections rather than encoders being active heat sources.

Fig. 2(*e*) demonstrates the stability of the microscope after closing the interferometer–scanner loop in PowerPMAC. Initially, when in open loop, 30 nm h^{-1} drift was observed after 1 h of pumping due to the thermal equilibration process. When the interferometer–sample scanner loop was closed in Delta Tau the system became stable for the entire duration of the experiment. The stability was verified through independent readings of the interferometer data through a native AttoFPSensor controls system software, which is completely independent of the motion controller position readings. The excellent stability of the microscope observed in the laboratory has been confirmed through synchrotron measurements as described in the next section.

4. Synchrotron experiments: ptychography, fluorescence and DPC imaging

Following extensive laboratory characterization, the MLL microscope was tested at the I13 beamline at Diamond Light Source. The system was temporarily installed in the c-hutch of the coherence branch of the beamline that is located inside a remote satellite building designed for high vibrational and temperature stability. The beamline employs horizontal geometry for high-heat-load optics in order to achieve high X-ray beam stability. A four-bounce fixed-exit water-cooled monochromator and a Rh stripe on the water-cooled harmonic rejection mirror were used to produce 11.8 keV monochromatic X-rays for the experiment. To increase the photon flux a set of Be compound refractive lenses (CRLs) was placed 25 m from the X-ray source. A large granite block (1.6 m × 1.2 m × 0.85 m and 4.4 metric tons) was used to support the MLL microscope and ensure damping of possible high-frequency vibrations. Ptychography, fluorescence and DPC imaging were performed under ambient conditions to characterize two-dimensional nanofocusing of the MLL microscope. The beam-defining slits selected coherent X-rays of 45 µm × 55 µm, which match the aperture of two orthogonally aligned MLLs. For ptychography measurements, a 10 µm × 10 µm order-sorting aperture (OSA) was introduced to allow only first-order focused beam to pass through. A 1 µm-thick gold Siemens star test pattern was positioned and scanned near the focal plane. The dwell time at each scan position was 1 s. Far-field diffraction patterns were collected by a Timepix pixel area detector (Llopart *et al.*, 2007) (512 × 512 pixels, 55 µm pixel size) located 0.85 m away from the sample. The ptychography scans covered 2 µm × 2 µm area following a Fermat spiral trajectory (Huang *et al.*, 2014) with 63 nm radial increment steps; the entire ptychography scan consisted of 325 diffraction patterns. Including overhead time, duration of the measurement was ∼13 min. Interferometric readout of the sample location was employed to fully reconstruct a 512 × 512 real-space image with 500 iterations of the Difference Map algorithm (Thibault *et al.*, 2008). This procedure yielded a pixel size of about 3 nm for the obtained real-space image. By propagating the reconstructed X-ray wavefront and monitoring the beam width at each propagation position, the horizontal and vertical focal planes were found to be separated by about 18 µm. The foci were determined to be 13.3 nm and 32.9 nm for horizontal and vertical focal planes, respectively, as shown in Fig. 3. Ptychography reconstructions exhibited the nanofocusing properties of the MLL optics and confirmed the high stability of the microscope.

Fig. 4(*a*) shows an scanning electron microscope (SEM) image of a fabricated Pt test pattern with line width varying between 20 and 30 nm. Figs. 4(*b*) and 4(*c*) show fluorescence and differential phase contrast images (Yan *et al.*, 2013) of the very same test pattern. The fluorescence images were acquired by raster scanning and recording intensity of the *Lα* emission line of Pt. In Figs. 4(*b*) and 4(*c*) the horizontal and vertical axis correspond to slow and fast scanning directions, respectively. The scan step size equalled 10 nm with 1 s dwell time and overhead time needed for repositioning, yielding overall data acquisition time of ∼10 h. Visual comparison between SEM and X-ray images exhibit excellent correlation, as shown in

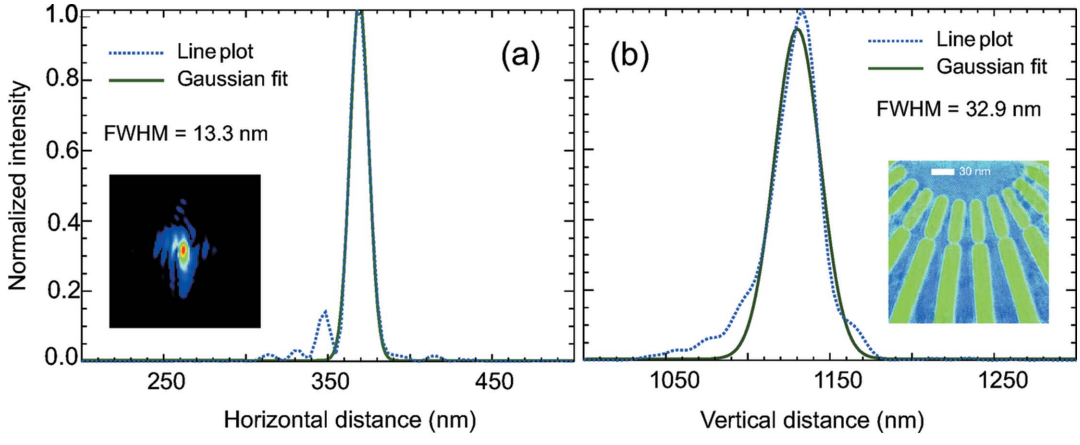

Figure 3
(*a*) Results of ptychography measurements: (*a*) Line focus in the horizontal direction, FWHM = 13.3 nm; the inset shows the shape of a probe. (*b*) Line focus in the vertical direction, FWHM = 32.9 nm. The dotted line shows reconstructed results, and the solid line shows a Gaussian fit. The inset demonstrates a two-dimensional reconstruction.

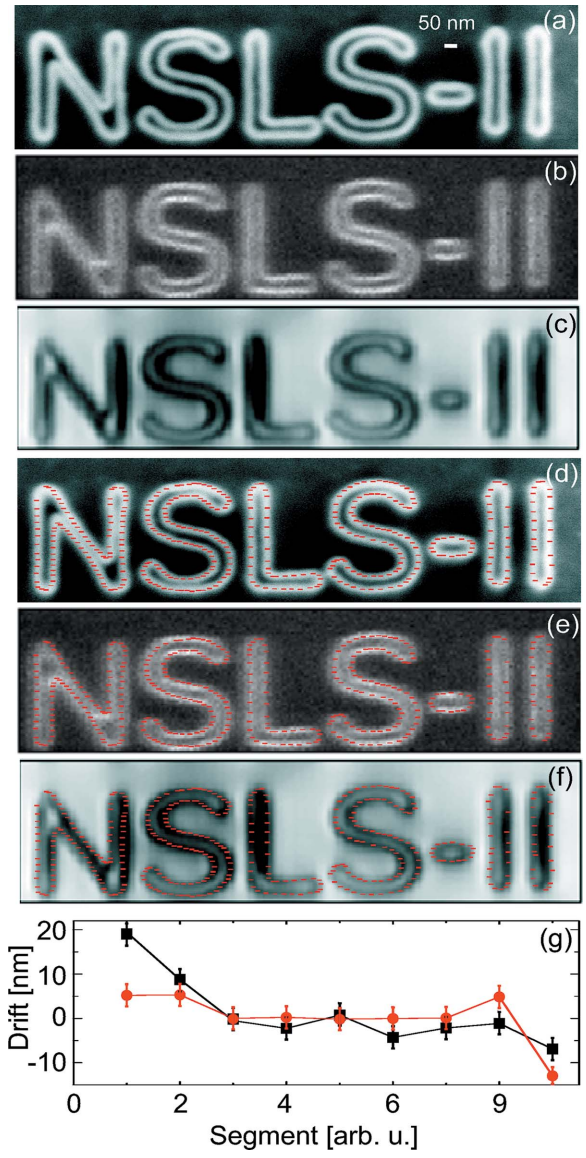

Figure 4
(*a*) SEM image of a test pattern used during synchrotron experiments. (*b*) Fluorescence image, (*c*) DPC image. Panels (*d*)–(*f*) show the same SEM, fluorescence and DPC images with red dots representing contours of the test pattern and directly superimposed on top of these images. (*g*) Drift during measurements derived from direct comparison between SEM and fluorescence images; squares represent the *x*-direction and circles the *y*-direction.

Fig. 4(*f*); red dotted lines mark the contours of the SEM image which are superimposed on fluorescence and DPC images. Prior to the comparison of fluorescence and SEM images, two misalignments were corrected: translational misalignment [using a sub-pixel registration method with 0.1 pixel accuracy (Guizar-Sicairos *et al.*, 2008)] and rotational discrepancy (corrected by rotating one image relative to the other one and maximizing cross correlation). To quantitatively verify the stability of the MLL microscope, SEM and fluorescence images were directly compared. The SEM image was used as a reference for normalization and position registration. Both SEM and fluorescence images were split into eight segments along the X-ray slow scan direction. We chose eight segments to have estimates for drifts during a ∼1 h time period. Each segment pair was directly compared and drift values during data acquisition were calculated using the same sub-pixel registration method as mentioned above (Guizar-Sicairos *et al.*, 2008). Relative drifts in both *x* and *y* directions in all eight segments were derived. Results of the comparison are shown in Fig. 4(*g*), yielding drift values of ∼2.5 nm h^{-1} and ∼2 nm h^{-1} for the *x* and *y* directions, respectively. The long-term fluorescence and DPC measurements confirmed the stability and reliability of the developed MLL system.

5. Conclusion

In conclusion, we have designed and constructed a dedicated X-ray microscope suitable for nanoscale imaging using MLL optics in the hard X-ray regime. Through thorough analysis and laboratory characterization of individual components, we were able to minimize thermal drifts and instabilities of the instrument down to the ∼2 nm h^{-1} level. We then illustrated the performance of the MLL-based microscope by performing ptychography, DPC and fluorescence imaging at a synchrotron facility and achieving two-dimensional nanometer-scale imaging resolution.

We thank Dr Deming Shu (ANL) for stimulating discussions. We acknowledge B. Mullany (BNL) for help with three-dimensional modelling of the microscope and D. Kuhne (BNL) for machining/assembling of mechanical parts. Work at Brookhaven was supported by the US Department of Energy under Contract No. DE-AC02-98CH10886. Fabrication of the test pattern and MLL post-growth processing was performed in part at the Center for Functional Nanomaterials, Brookhaven National Laboratory, supported by the US Department of Energy, Office of Basic Energy Sciences, under Contract No. DE-AC02-98CH10886. Work at Argonne was supported by the US Department of Energy, Office of Science, under Contract No. DE-AC02-06CH11357. We acknowledge Diamond Light Source Ltd for providing beam time at I13L.

References

Bukhard, K., Pierre, T., Alessandra, G. & Maya, K. (2011). *J. Phys. Condens. Matter*, **23**, 083002.
Chen, T. Y., Chen, Y. T., Wang, C. L., Kempson, I. M., Lee, W. K., Chu, Y. S. & Margaritondo, G. (2011). *Opt. Express*, **19**, 19919.
Evans-Lutterodt, K., Stein, A., Ablett, J. M., Bozovic, N, Taylor, A. & Tennant, D. M. (2007). *Phys. Rev. Lett.* **99**, 1348001.
Gofron, K., Lauer, K., Nazaretski, E., Yan, H., Kalbfleisch, S., Greer, A., Dalesio, R. & Chu, Y. S. (2014). *J. Phys. Conf. Ser.* **493**, 012026.
Guizar-Sicairos, M., Thurman, S. T. & Fienup, J. R. (2008). *Opt. Lett.* **33**, 156–158.
Huang, X., Yan, H., Harder, R., Hwu, Y., Robinson, I. K. & Chu, Y. S. (2014). *Opt. Express*, **22**, 12634–12644.
Huang, X., Yan, H., Nazaretski, E., Conley, R., Boet, N., Zhou, J., Lauer, K., Li, L., Eom, D., Legnini, D., Harder, R., Robinson, I. K. & Chu, Y. S. (2013). *Sci. Rep.* **3**, 3562.
Ice, G. E., Budai, J. D. & Pang, W. L. (2011). *Science*, **334**, 1234.
Kang, H. C., Maser, J., Stephenson, G. B., Liu, C., Conley, R., Macrander, A. T. & Vogt, S. (2006). *Phys. Rev. Lett.* **96**, 127401.

Lammle, K., Trevethan, T., Schwarz, A., Watkins, M, Shluger, A. & Wiesendanger, R. (2010). *Nano. Lett.* **10**, 2965–2971.
Llopart, X., Ballabriga, R., Campbell, M., Tlustos, L. & Wong, W. (2007). *Nucl. Instrum. Methods Phys. Res. A*, **581**, 485–494.
Meckler, S., Gyamfi, O., Pietzsch, O. & Wiesendanger, R. (2009). *Rev. Sci. Instrum.* **80**, 23708.
Mesaros, A., Fujita, K., Eisaki, H., Uchida, S., Davis, J. S., Sachdev, S., Zaanen, J., Lawler, M. J. & Kim, E.-A. (2011). *Science*, **333**, 426–430.
Mimura, H., Handa, S., Kimura, T., Yumoto, H., Yamakawa, D., Yokoyama, H., Matsuyama, S., Inagaki, K., Yamamura, K., Sano, Y., Tamasaku, K., Nishino, Y., Yabashi, M., Ishikawa, T. & Yamauchi, K. (2010). *Nat. Phys.* **6**, 122–125.
Nazaretski, E., Graham, K. S., Thompson, J. D., Wright, J. A., Pelekhov, D. V., Hammel, P. C. & Movshovich, R. (2009). *Rev. Sci. Instrum.* **80**, 83704.
Nazaretski, E., Huang, X., Yan, H., Lauer, K., Conley, R., Bouet, N., Zhou, J., Xu, W., Eom, D., Legnini, D., Harder, R., Lin, C.-H., Chen, Y.-S., Hwu, Y. & Chu, Y. S. (2014). *Rev. Sci. Instrum.* **85**, 33707.
Nazaretski, E., Kim Jungdae, Yan, H., Lauer, K., Eom, D., Shu, D., Maser, J., Pesic, Z., Wagner, U., Rau, C. & Chu, Y. S. (2013). *Rev. Sci. Instrum.* **84**, 33701.
Schroer, C. G., Kurapova, O., Patommel, J., Boye, P., Feldkamp, J., Lengeler, B., Burghammer, M., Riekel, C., Vincze, L., van der Hart, A. & Küchler, M. (2005). *Appl. Phys. Lett.* **87**, 124103.
Shu, D., Nazaretski, E., Kim, J., Yan, H., Lauer, K., Mullany, B., Kuhne, D., Maser, J. & Chu, Y. S. (2013). *J. Phys. Conf. Ser.* **463**, 12029.
Thibault, P., Dierolf, M., Menzel, A., Bunk, O., David, C. & Pfeiffer, F. (2008). *Science*, **321**, 379–382.
Vila-Comamala, J., Gorelick, S., Färm, E., Kewish, C. M., Diaz, A., Barrett, R., Guzenko, V. A., Ritala, M. & David, C. (2011). *Opt. Express*, **19**, 175.
Wu, H. R., Chen, T. S., Chu, Y. S., Conley, R., Bouet, N., Chien, C. C., Chen, H. H., Lin, C. H., Tung, H. T., Chen, Y. S., Margaritondo, G., Je, J. H. & Hwu, Y. (2012). *J. Phys. D*, **45**, 242001.
Yan, H., Chu, Y. S., Maser, J., Nazaretski, E., Kim, J., Kang, H. C., Lombardo, J. J., Gofron, K. & Chiu, W. K. S. (2013). *Sci. Rep.* **3**, 1307.
Yan, H., Conley, R., Bouet, N. & Chu, Y. S. (2014). *J. Phys. D*, **47**, 263001.
Yan, H., Rose, V., Shu, D., Lima, E., Kang, H. C., Conley, R., Liu, C., Jahedi, N., Macrander, A. T., Stephenson, G. B., Holt, B., Chu, Y. S., Lu, M. & Maser, J. (2011). *Opt. Express*, A**19**, 15069–15076.